Electronic Supplementary Material (ESI) for Nanoscale.
This journal is © The Royal Society of Chemistry 2016

Inherent Predominance of High Chiral Angle Metallic Carbon Nanotubes in Continuous Fibers Grown From Molten Catalyst

B. Alemán,[a] M. Mar Bernal, [b] B. Mas, [a] Emilio M. Pérez,[b] V. Reguero,[a] G. Xu, [a] Y. Cui, [a] Juan J. Vilatela†[a]

[a]IMDEA Materials Institute, c/ Eric Kandel 2, Getafe 28906, Madrid, Spain.

[b]IMDEA Nanoscience Institute, c/Faraday 9, Ciudad Universitaria de Cantoblanco, 28049, Madrid, Spain.

† Corresponding author: juanjose.vilatela@imdea.org

S1. RBM region of the Raman spectra of CNT fibers and its relation to the complete SWNT landscape. Figure S1.a shows the complete Katura Plot of possible SWNTs, with armchair CNTs marked in pink and different laser lines indicated. Figure 1Sb shows the RBMs observed with a 785nm laser line, with the highest intensity peak corresponding to M CNTs. To illustrate the limitations of Raman spectroscopy to assign chiral angles in samples with a large number of different CNTs, In Figure 1Sc we superimpose the 50meV resonance window onto the corresponding region of the Kataura plot. The comparison shows the small fraction of SWNTs probed with the laser.

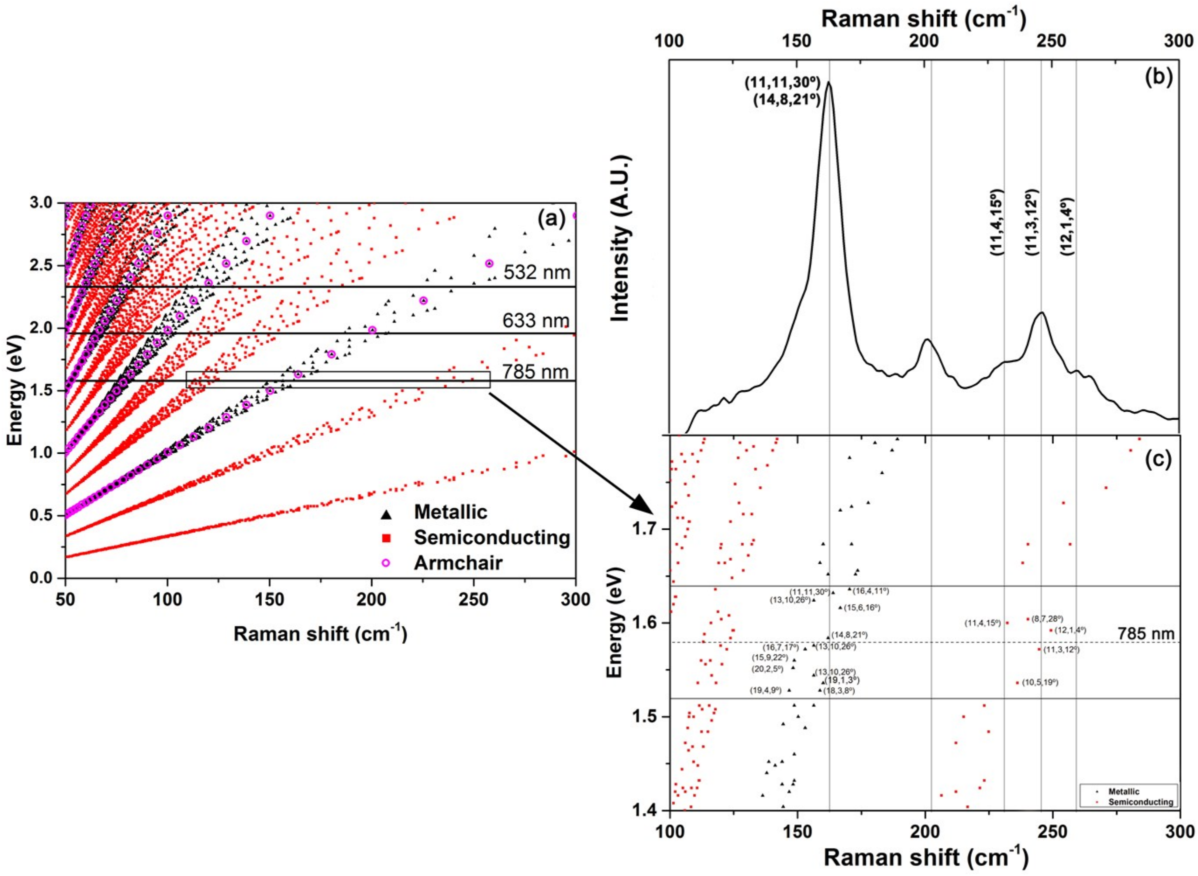

Figure S1. (a) Kataura Plot with (CNTs corresponding to armchair chiral angle marked in pink). (b) RBM Raman shifts obtained by 785 nm laser excitation and its (c) correspondance with the Kataura Plot SWNT landscape.

S2. CNT fiber preparation for UV-vis-NIR and photoluminescence spectroscopies. CNT fiber filaments were shortened down to ~100 μm by ion milling in a Focus Ion Beam microscope and then dispersed in sodium dodecyl sulfate (SDS) for subsequent absorption and emission spectroscopy measurements. Electron and optical images of the shortened fibers are shown in Figure S2.

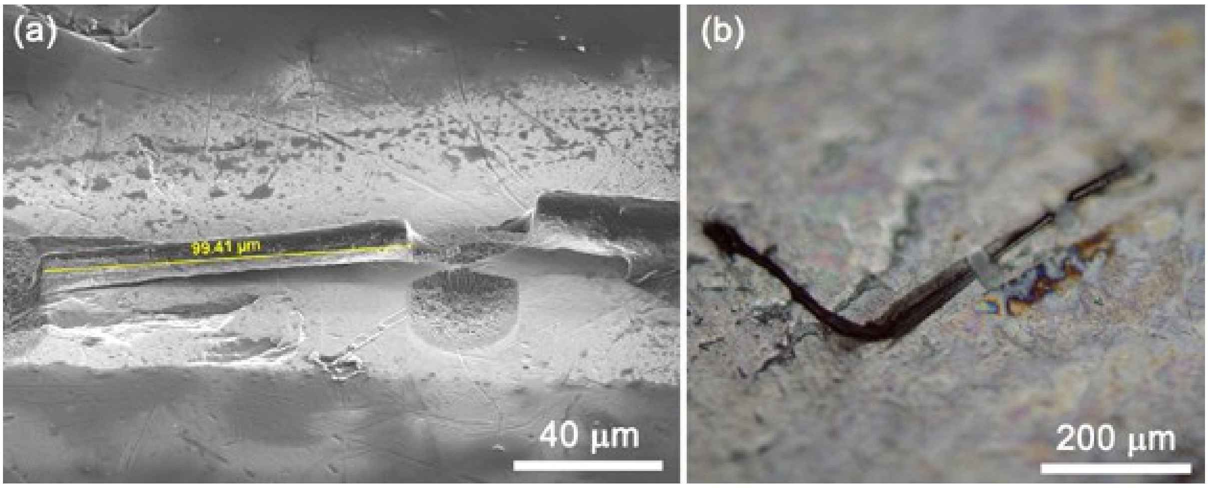

Figure S2. (a) Electron and (b) optical images of a 100 m long CNT fiber filament for absorption/emission studies in dispersion in SDS.

S3. CNT fiber fluorescence map.

Figure S3 shows the fluorescence intensity of the CNT fiber as function of the excitation and emission wavelength. Rayliegh scattering has not been filtered. The absence of emission signals confirms the negligible presence of SC-SWNTs in the fiber.

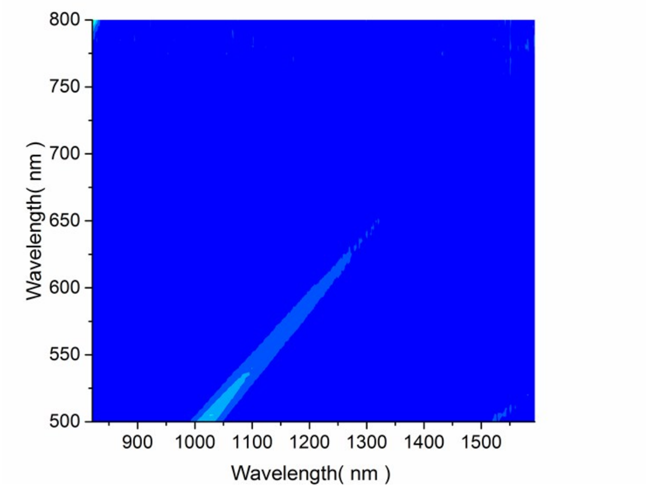

Figure S3. CNT fiber fluorescence map as function of the excitation and emission wavelength.

S4. Chiral angle assignment to CNT bundles extracted from electron diffraction patterns.

Most chiral angles can be directly extracted from the diffraction pattern by simple image analysis. However, when the presence of misaligned CNTs or different chiral angles broadens the diffraction spots, we determine chiral angles from azimuthal profiles obtained by radial integration. By measuring the angle (θ) between the (002) and {100} type reflections, the chiral angle corresponds to $\chi=90°-\theta$.

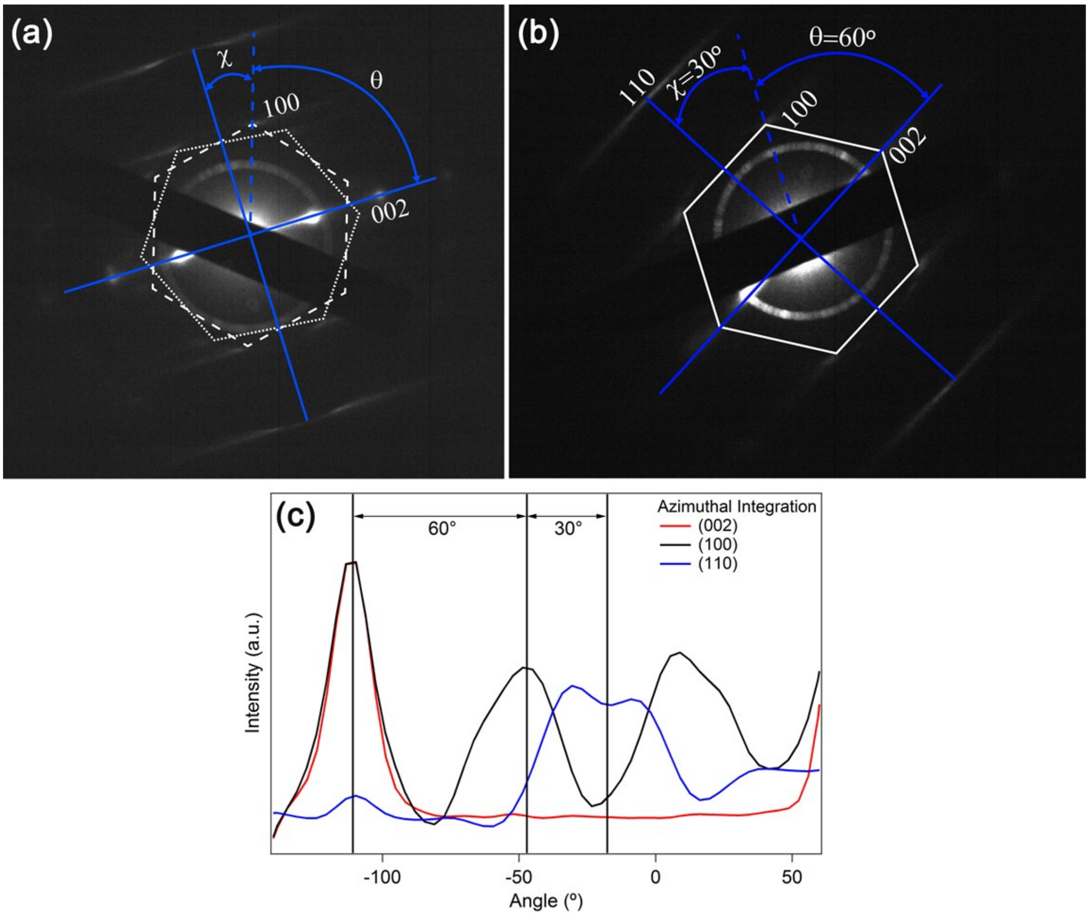

Figure S4. (a) Chiral and (b) armchair CNT bundles SAED patterns. (c) Azimuthal integration of {002}, {100} and {110} reflections for armchair CNT bundle.

S5. CNT chiral angle using toluene as carbon source or Se as promotor.

Figure S5-Ia shows a CNT bundle TEM image of a fiber synthesized using toluene as C source with its corresponding SAED pattern (Figure S5-Ib). Azimuthal integration of the different reflections (S5) results in a chiral angle distribution around 30±6° (armchair/nearly armchair).

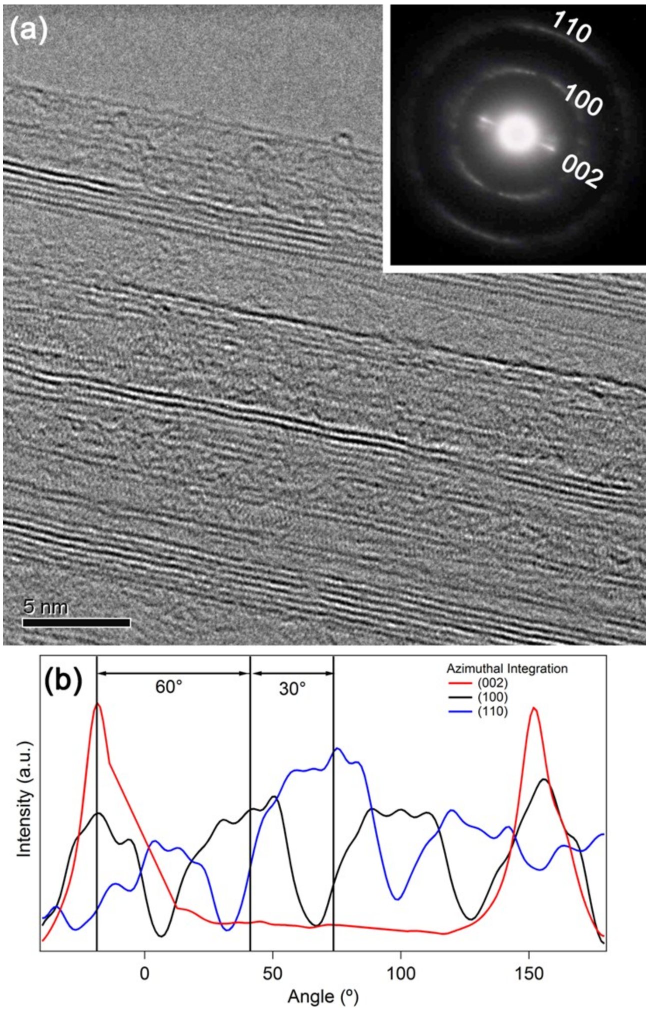

Figure S5-I (a) HRTEM image of a CNT bundle of a fiber produced with toluene and its SAED pattern (inset). (b) Azimuthal integration of the SAED pattern for chiral angle assignation.

Similarly, Figure S5-II shows the SAED chiral angle distribution obtained from a fiber of SWNTs grown using butanol as carbon source and Se as promotor, and an example of a SAED pattern of an armchair CNT.

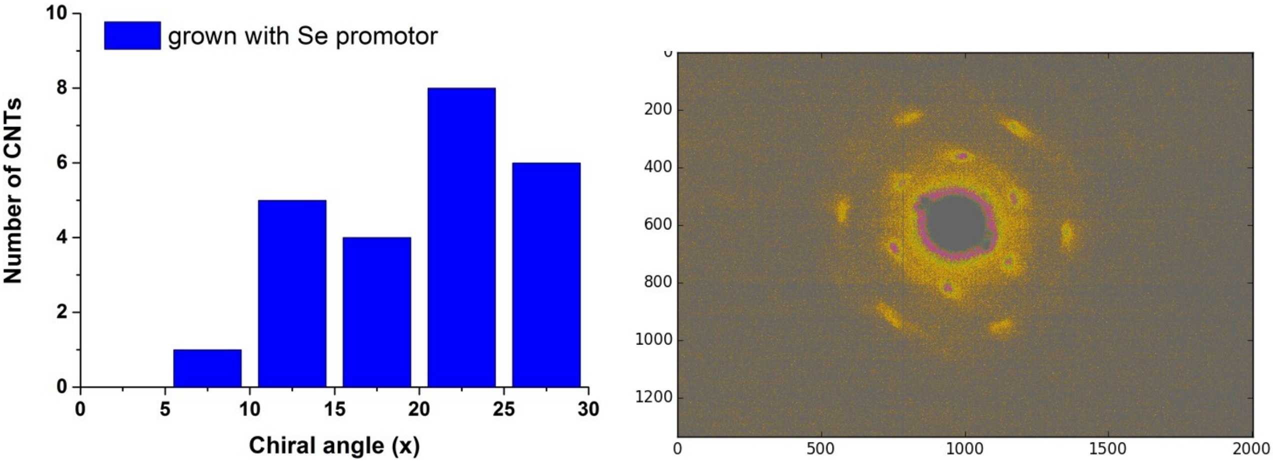

Figure S5-II. Distribution of CNT chiral angles in fibers produced using Se as promotor instead of S (top) and example of a SAED pattern for an armchair CNT.

S6. Post-synthesis catalyst characterization.

The ratio S/Fe was measured by EDS on large samples of CNT fibers in the SEM, using a voltage of 15kV. The Figure below presents an example of an EDS spectrum showing peaks corresponding to S and Fe, as well as small signals from the sample holder and adhesive tape (Al, O, Cu) as well as contaminants from the paper used during collection (Ca, Cl, O) and particulate fragments from the reactor tube (SiO_x), but which do not intervene in the catalyst reaction. The atomic ratio can be directly obtained by comparison of intensity signals with respect to standard samples, which the software carries out automatically. Similar EDS measurements on samples produced with increasing amount of S precursor show a corresponding increase in the S/Fe, that thus rule out the possibility of the S originating from impurities.

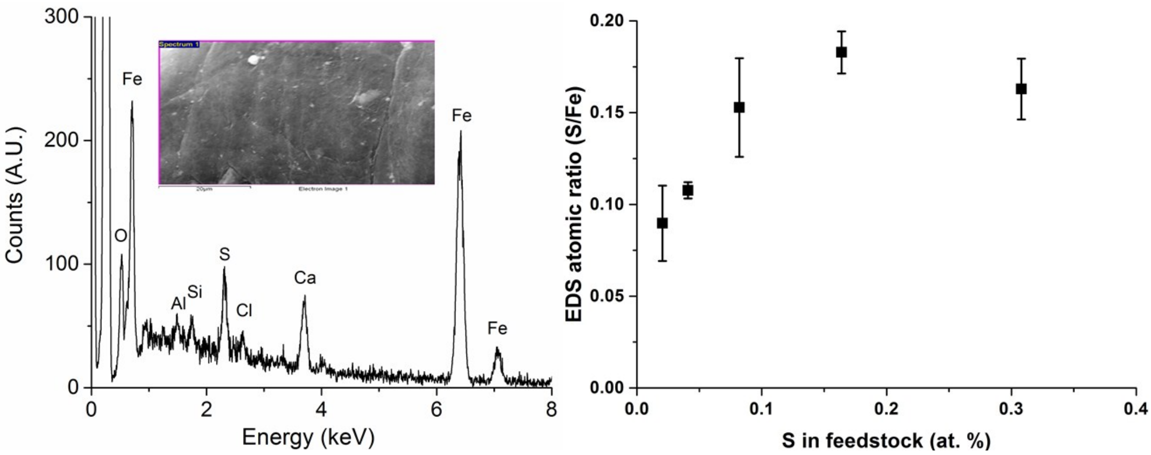

Figure S6-I. EDS spectra showing the presence of S and Fe in the catalysts (left). Increase in S/Fe ratio with increasing content of S precursor during synthesis (right).

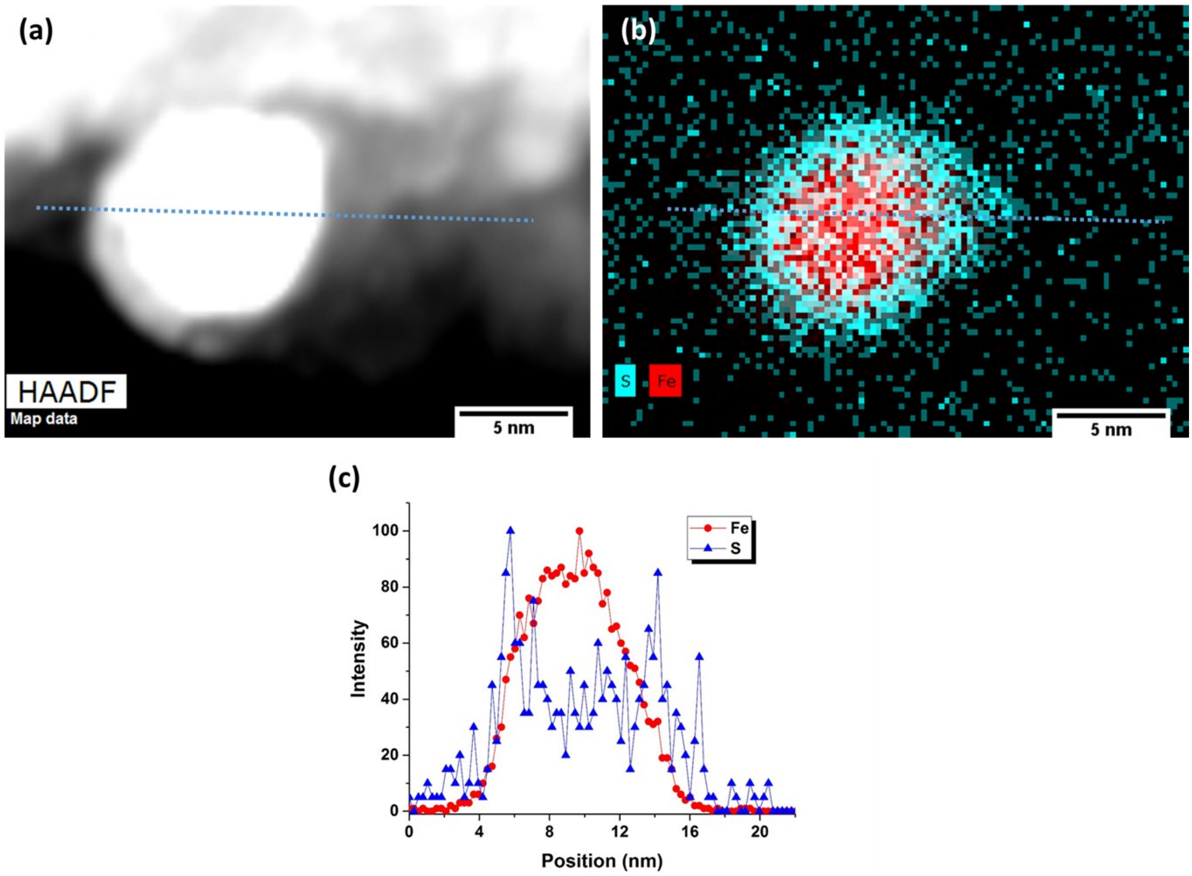

Figure S6-II. STEM micrograph (a) and EDS map (b) showing the presence of S at the surface of the Fe-rich catalysts. The intensity line profile across the particle (c) shows higher S concentration at the particle edged, implying higher concentration of S at the surface of the particle.

Figure S6-II presents an example of a high magnification STEM micrograph of a catalyst particle and the corresponding EDS compositional data. In Figure S6-IIb, the map of superimposed Fe and S signals shows the semicircular line shape of the Fe signal reflecting the shape of the particle and a homogeneous Fe concentration. The S line is clearly more intense at the edges of the particle therefore indicating a higher concentration at the surface. Such structure is confirmed by plotting the Fe and S signal intensities (i.e. concentration) across the particle, as shown in Figure S6-IIc. These data also show in passing that S is only associated to the catalyst particles.

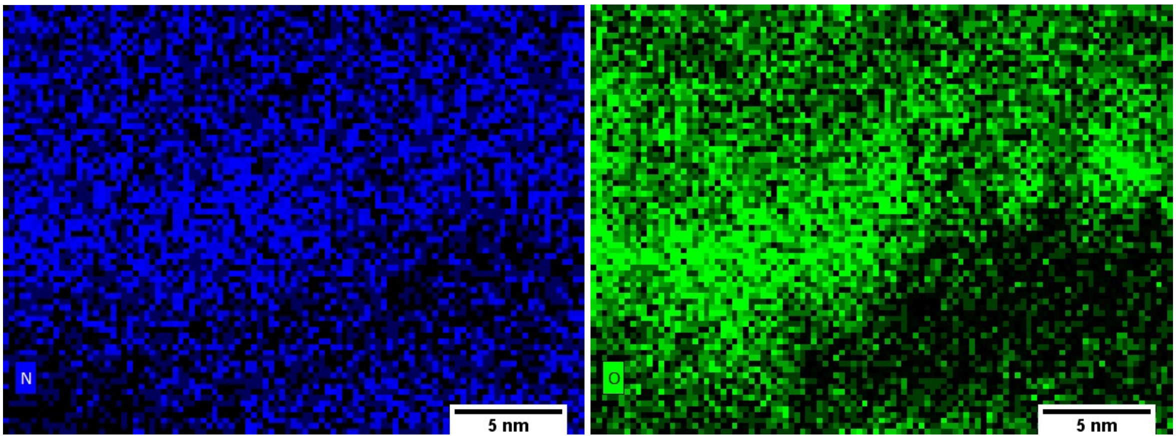

Figure S6-III. STEM EDS maps for N and O for the same region as in Figure S6-II (a). The comparison confirms that O is only detected as background and that the catalyst is not oxidised.

An EDS map for O in Figure 6-III is also included to rule out the presence of an oxidised (FeO_x) catalyst. We compare this map to that for an arbitrary element that is known not to be present in the sample, N. The maps are nearly identical, corresponding only to background noise and confirming that there is no appreciable O in the catalyst. The presence of oxidised catalyst is further ruled out by XPS and Raman measurements on bulk samples, as discussed below.

Unlike conventional CVD in which pre-deposited catalyst is often oxidised during transportation to the CVD reactor due to direct contact with air, virtually all the catalyst in our samples is metallic because it is encapsulated by a graphite layer that prevents oxidation. We have confirmed this by carrying out Raman spectroscopy on fibre samples before and after pyrolysis in air at 600C for 1h. To avoid uncertainty in assigning low frequency Raman modes to CNT RBMs or FeO_x, we have used a samples of MWNTs for this experiments, although very small contributions from SWNTs could still be observed. The comparison of spectra below shows clearly the Raman modes from Fe_2O_3 (224-A_{1g}, 243-E_g, 290-E_g, 408-E_g, 496-E_g, 609-E_g, 659-E_u)[1], none of which are present in the CNT fibre sample.

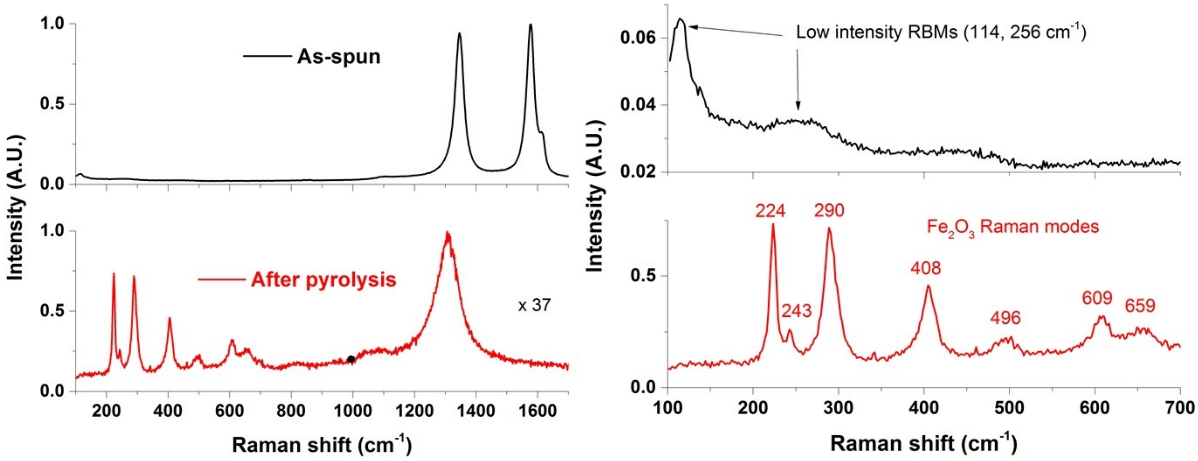

Figure S6-IV. Raman spectra of CNT fibre material as-spun and after pyrolysis to induce oxidation of the catalyst. The comparison confirms that the catalyst is metallic.

XPS data.

The Fe2p3/2 core level emission at 711 eV is assigned to the presence of FeS compounds. As Figure S6-V shows, the increment of thiophene (S precursor) in the solution translate into an increase of the Fe2p3/2 at 711 eV and Fe2p1/2 at 725 eV relative intensity with respect to metallic Fe. Furthermore, the S2p emission region presents two components at 162 and 169 eV that agree with the formation of sulphur compounds[2].

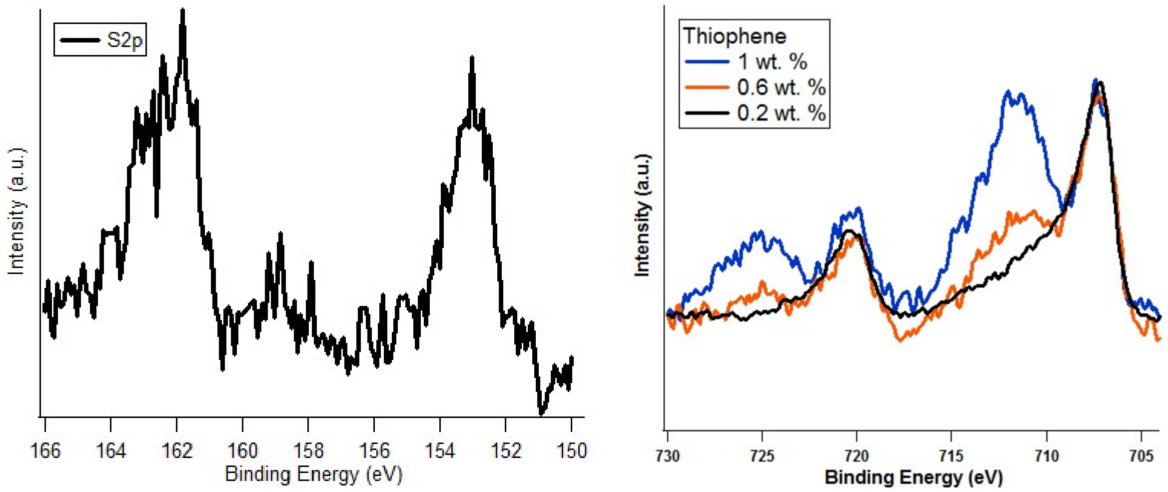

Figure S6-V. XPS spectra showing the presence of sulphur (left) and confirming the formation of a Fe-S intermetallic (right).

XPS data can also rule out the presence of oxidised catalyst. The effect of iron oxides on the O1s core level emission is a downshift in binding energies to around 530 eV[3]. In the SWNT fibre the O1s emission presents an intense broad component at 532.7 eV and a shoulder at 537 eV, which correspond to different C/O species[4,5] such as as C-O, C=O and physisorbed O2. Overall, the concentration of C/O species in the fibre is very low compared to the sp2 hybridized carbon, as indicated by high intensity narrow C1s core level emission peak at 284.5 eV (sp2), with only a slight broadening at higher binding energies (C-O: 285 eV and C=O: 288 eV) and the pi-pi*interaction at 290.5 eV.

Crystal structure and compositions of the catalyst particles

The FCC Fe phase predominance in the catalyst particles is observed by HRTEM and XRD measurements, as shown in Figure S6-III .

The identification of the crystal phase is performed through the inverse-FFT filtering of the most intense spots related to the catalyst of the FFT. The FFT and the inverse-FFT processed image are then compared to different (FCC Fe, BCC Fe, Fe-C compounds and Fe-S compounds) simulated SAED patterns and crystal structures by *Crystal Maker and Single Crystal software*.

The figure below presents a HRTEM image of catalyst particle with a well resolved set of crystal planes. Due to the size and shape of the catalyst particle and the presence of graphitic carbon the FFT shows an overlap of spots, therefore only those planes related to [1 -1 0] zone axis are used for assignation.

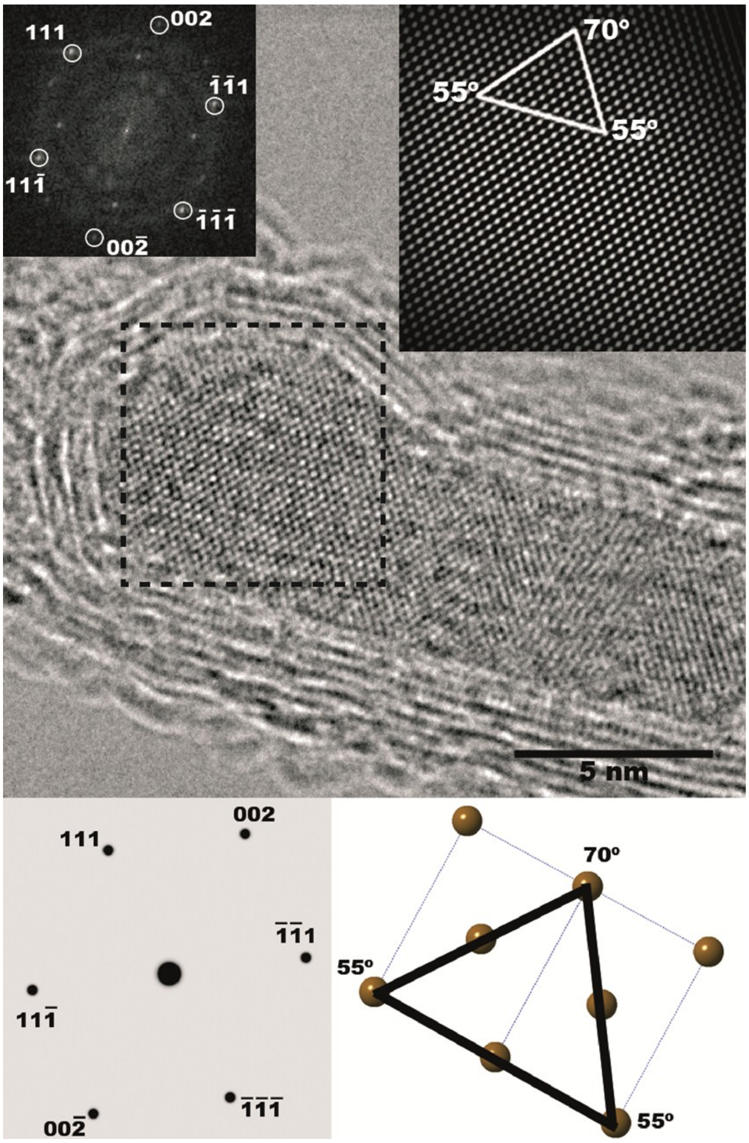

Figure S6-VI. High-resolution TEM micrograph of an active catalyst particle with the corresponding FFT and the assignation to fcc Fe.

The next histogram shows the distribution from the different crystal phases found in 24 HRTEM with sufficient resolution for this analysis, but out of many more observations. The middle bar corresponds to the cases when it is not possible to distinguish between BCC Fe and FCC Fe or Graphitic C. The carbide is observed typically for larger diameter particle is clearly infrequent.

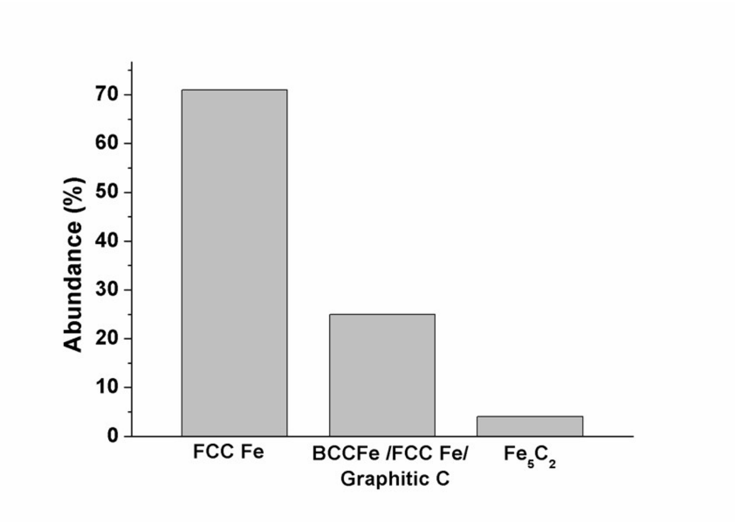

Figure S6-VII. Histogram showing fcc Fe as the most abundant catalyst structure based on HRTEM observations on over 24 active catalyst particles.

Figure S6-VIII presents XRD data for a SWNT fibre sample, obtained by azimuthal integration of a 2D WAXS pattern obtained using synchrotron radiation at the non-crystalline diffraction NCD line of Alba light source. The sample consisted of an array of 100 filaments of CNT fibre in parallel so as to increase scattering intensity.

The radial profile, equivalent to a “powder” diffraction pattern, confirms the predominance of fcc Fe.

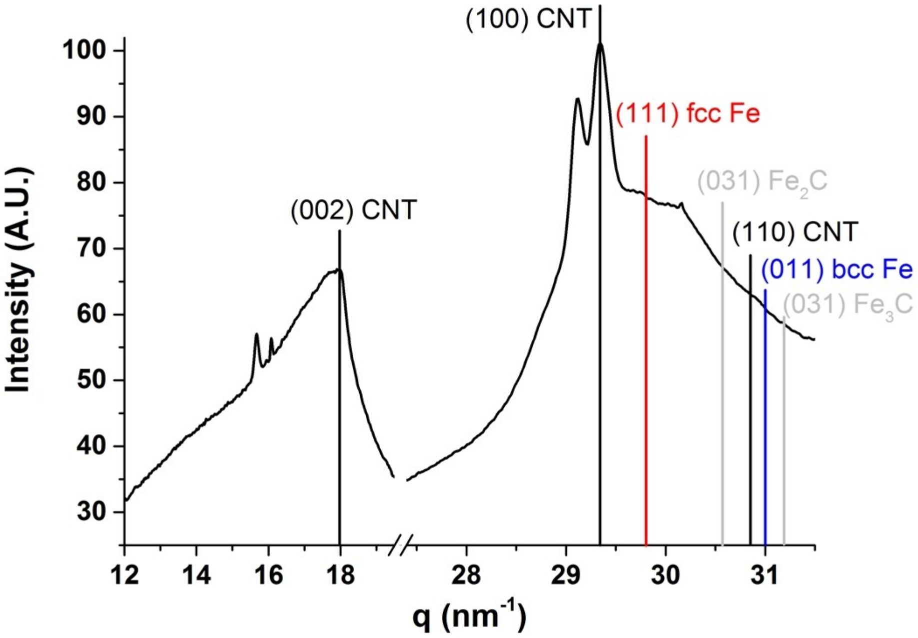

Figure S6-VIII. XRD pattern of a SW CNT fiber including the most intense peak for fcc-Fe, bbc-Fe, Fe_3C and F_2C. The pattern is consistent with a large fraction of fcc-Fe particles observed by HRTEM.

Figure S6-IX shows a plot of the thickness of an Fe-S intermetallic layer calculated for a 2nm-diameter particle as a function of S concentration. In the range determined experimentally (<10 at.%), this shell corresponds to a subnanometric layer that cannot therefore be detected by X-ray or electron diffraction. The unit cell of FeS and a schematic of a quarter of the catalyst on the same scale are also included for reference.

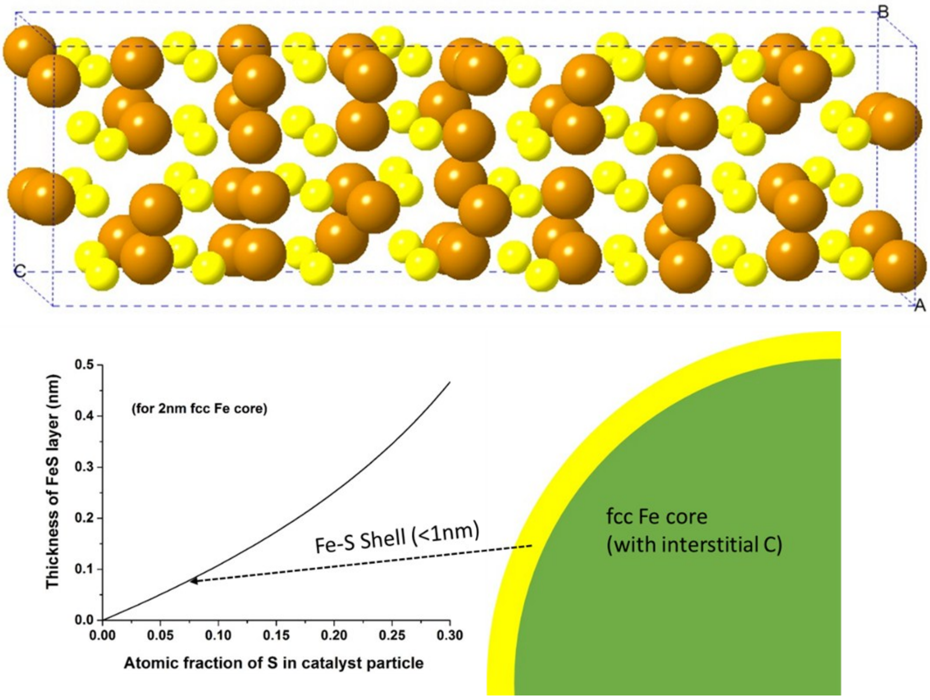

Figure S6-IX. Schematic comparing the unit cell of FeS and the calculated size of the FeS layer in the catalyst particle.

S7. Phase diagrams and the proposed evolution of the alloy catalyst particle.

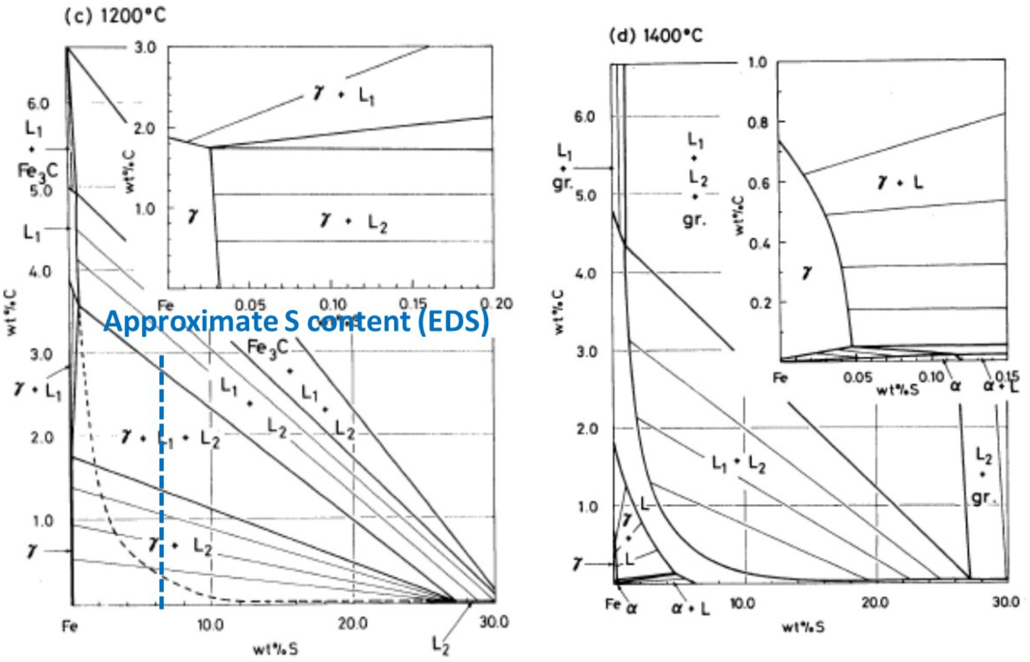

Figure S7-I Isothermal sections of calculated ternary diagram. Modified from reference [6].

Plot of cooling rate calculated from the temperature profile at the lower end of the CVD reactor tube.

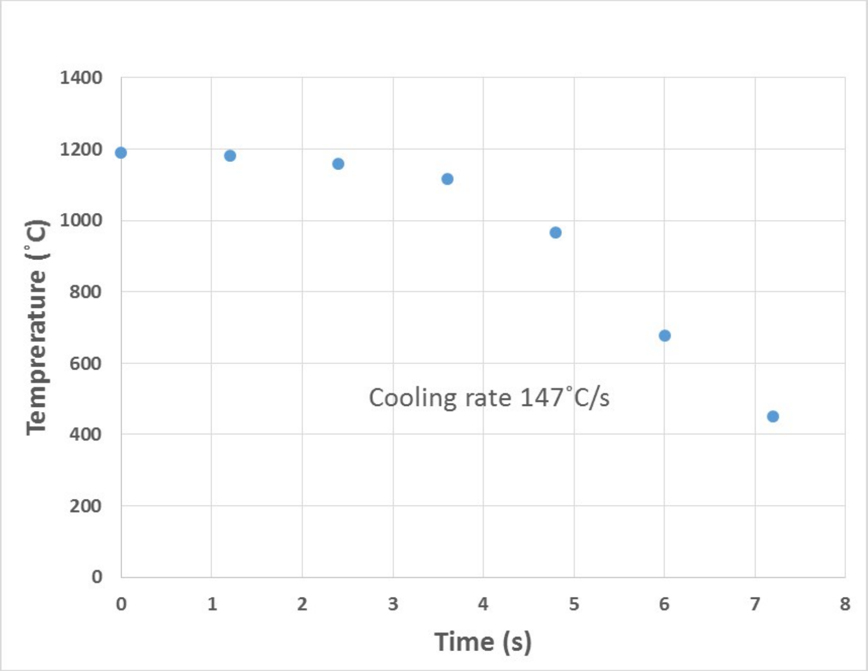

Figure S7-II. Plot of approximate temperature of a particle flowing across the CVD reactor. Temperature values are calculated from the temperature profile and assuming thermal equilibrium. The cooling rate corresponds to the steepest part of the curve.

(1) Shim, S.-H.; Duffy, T. S. Raman Spectroscopy of Fe $_2$ O $_3$ to 62 GPa. *Am. Mineral.* **2002**, *87*, 318–326.

(2) *Handbook of X-Ray Photoelectron Spectroscopy: A Reference Book of Standard Spectra for Identification and Interpretation of XPS Data*; Moulder, J. F.; Stickle, W. F.; Sobol, P. E.; Bomben, K. D.; Chastain, J.; King Jr., R. C.; Physical Electronics, Incorporation, Eds.; Physical Electronics: Eden Prairie, Minn., 1995.

(3) Fujii, T.; de Groot, F. M. F.; Sawatzky, G. A.; Voogt, F. C.; Hibma, T.; Okada, K. *In Situ* XPS Analysis of Various Iron Oxide Films Grown by NO 2 -Assisted Molecular-Beam Epitaxy. *Phys. Rev. B* **1999**, *59*, 3195–3202.

(4) Liu, T.; Yang, F.; Li, Y.; Ren, L.; Zhang, L.; Xu, K.; Wang, X.; Xu, C.; Gao, J. Plasma Synthesis of Carbon Nanotube-Gold Nanohybrids: Efficient Catalysts for Green Oxidation of Silanes in Water. *J Mater Chem A* **2014**, *2*, 245–250.

(5) Tillborg, H.; Nilsson, A.; Hernnäs, B.; Mårtensson, N.; Palmer, R. E. X-Ray and UV Photoemission Studies of Mono-, Bi- and Multilayers of Physisorbed Molecules: O2 and N2 on Graphite. *Surf. Sci.* **1993**, *295*, 1–12.

(6) Ohtani, H.; Nishizawa, T. Calculation of Fe-C-S Ternary Phase Diagram. *Trans. Iron Steel Inst. Jpn.* **1986**, *26*, 655–663.